

Prediction of High Curie Temperature, Large Magnetic Crystal Anisotropy, and Carrier Doping-Induced Half-Metallicity in Two-Dimensional Ferromagnetic FeX₃ (X = F, Cl, Br, and I) Monolayers

Zhaoyong Guan* and Shuang Ni

Cite This: *J. Phys. Chem. C* 2021, 125, 16700–16710

Read Online

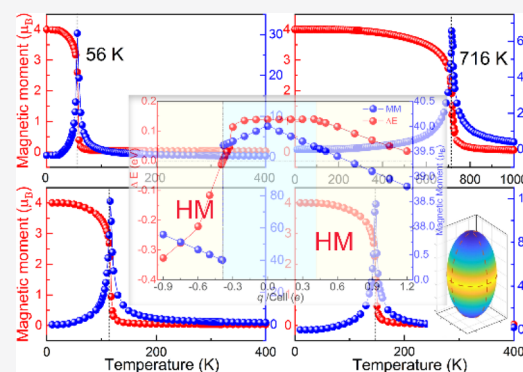
ACCESS |

Metrics & More

Article Recommendations

Supporting Information

ABSTRACT: Two-dimensional (2D) intrinsic ferromagnetic (FM) semiconductors (SCs) are urgent for spintronics. FeX₃ (X = F, Cl, Br, and I) monolayers with intrinsic ferromagnetism are fabricated by density functional theory and confirmed by a global minimum search. FeX₃ (X = F, Cl, Br, and I) show a FM ground state, while an AFM-ZZ order has the second lowest energy. FeX₃ (X = F, Cl, Br, and I) have a Curie temperature (T_c) of 56, 716, 116, and 148 K, respectively. FeX₃ (X = F and Cl) are bipolar magnetic semiconductors (BMSs), while FeX₃ (X = Br and I) are half-semiconductors (HSCs). FeF₃ has a direct gap of 4.78 eV, while FeX₃ (X = Cl, Br, and I) have indirect band gaps of 2.92, 2.36, and 1.69 eV, respectively. They show perpendicular magnetic anisotropy, with a magnetic anisotropy energy (MAE) of 0.08, 0.11, 0.59, and 3.19 meV, respectively. All FeX₃ show good dynamical and thermal stability. Moreover, charge doping can transform FeCl₃ from the BMS with an FM order to a half-metal (HM) with ferrimagnetic (Ferrim) or FM orders. However, FeI₃ could be transformed from the HSC with an FM order into an HM with Ferrim or FM orders. The high T_c , large MAE, and tunable electromagnetic properties suggest that 2D FeX₃ (X = F, Cl, Br, and I) are promising magnetic SCs for potential application in electronics and spintronics.



1. INTRODUCTION

Since the discovery of graphene,¹ two-dimensional (2D) materials have showed attractive properties^{2,3} and played an important role in modern electronic,^{4,5} spintronic,^{6–8} and magnetoelectronic devices.⁹ Graphene shows interesting physical and electronic properties.⁴ Other 2D materials, such as hexagonal boron nitride,^{10,11} transition-metal dichalcogenides,^{12–14} and stanene,¹⁵ have been found and presented attractive physical properties.⁴ Most 2D materials are non-magnetic materials.¹⁴ Because the long-range magnetic order at a finite temperature in 2D materials is forbidden,¹⁶ 2D ferromagnetic (FM) materials have not appeared until recent years,^{6–8,17–21} which limits 2D materials' application in electronics and spintronics.²² 2D van der Waals materials with intrinsic ferromagnetism,^{6–8,17,18} such as CrI₃ (CrBr₃), Fe₃GeTe₂,²³ Cr₂Ge₂Te₆,^{24,25} and 2H-VSe₂,²⁶ have been successfully synthesized in the experiments. Cr₂Ge₂Te₆ and Fe₃GeTe₂ are FM materials with a T_c of 220²⁷ and 223 K,²² respectively. However, Cr₂Ge₂Te₆²⁴ and Fe₃GeTe₂²⁸ are metals, which restricts their wide application (such as field effect transistors) in electronics.²⁵ 2H-VSe₂ has a higher T_c of 300 K²⁹ with an intrinsic FM order,²⁶ but its magnetic order is related to the substrate.²⁶ In summary, magnetic semiconductors (SCs) are rare.³⁰ Moreover, the T_c of these FM materials is usually quite low.³⁰ The ferromagnetism in SCs

usually originates from d-p-d superexchange interaction. Therefore, it is quite weak, which hinders the wide application of 2D materials in spintronics.^{31,32} Tunable FM orders,^{33–35} semiconductive properties,³⁶ and high³⁷ T_c are expected in 2D magnetic materials.^{31,34,37} To increase T_c and improve magnetic stability,³⁸ researchers have tried to modulate,²² synthesize,^{6,26} and design various magnetic SCs.^{37–39}

CrI₃ van der Waals structures have been successfully synthesized in the experiment,^{7,40} and magnetic orders are dependent on the layers and stacking patterns.⁴¹ However, the corresponding T_c is much lower than room temperature.⁷ Therefore, many researchers have tried to increase T_c and control the magnetic properties of CrI₃.^{6,17–19,21} 2D materials and CrI₃ could form all kinds of vdW structures,^{6,8,17–21} which show amazing electronic,^{42,43} magnetic,^{20,44} and valleytronic properties.⁴⁵ One strategy is replacing I atoms in CrI₃ with Cl or Br atoms. A new phenomenon such as magneto-optical Kerr switching,⁴⁶ direct photoluminescence,⁴⁷ and critical region

Received: May 1, 2021
Revised: June 23, 2021
Published: July 27, 2021



phase transition⁴⁸ appears, and the corresponding T_c could be modulated ($T_c^{\text{CrBr}_3} = 41.3$ K and $T_c^{\text{CrCl}_3} = 29.7$ K).⁴⁹ What are the properties of MI_3 , when Cr and I atoms in CrI_3 are replaced by other transitional metals (Fe) and halogen atoms (F, Cl, Br, and I) in the meantime?

In this article, we perform a systematic study on FeX_3 ($X = \text{F, Cl, Br, and I}$) monolayer (MLs), using density functional theory and a global minimum search. The intrinsic ferromagnetism in FeX_3 originates from the superexchange interaction of Fe-X-Fe bonds. The energy difference of FeX_3 ($X = \text{F, Cl, Br, and I}$) between FM and AFM-ZZ orders is 0.011, 0.138, 0.023, and 0.029 eV, respectively. FeX_3 ($X = \text{F and Cl}$) are bipolar magnetic semiconductors (BMSs), while FeX_3 ($X = \text{Br and I}$) are half-semiconductors (HSCs). FeF_3 has a direct gap, while other FeX_3 have an indirect gap. The corresponding T_c is 56 (FeF_3), 716 (FeCl_3), 116 (FeBr_3), and 148 K (FeI_3), respectively. They all show perpendicular magnetic anisotropy (PMA) with large MAE. All FeX_3 show good dynamical and thermal stability. Charge doping could modulate FeCl_3 and FeI_3 from the BMS and HSC with an FM order to a half-metal (HM) with FM or Ferrim orders by changing super and direct exchange interaction, respectively. Our results will provide a view to understand magnetic and electronic properties of FeX_3 MLs, which is useful for the design of new nanoelectronic devices based on the FM SCs.

2. COMPUTATIONAL DETAILS

The geometry is searched by the particle-swarm optimization (PSO) method, implemented in the CALPSO code.⁵⁰ The plane-wave basis Vienna ab initio simulation package (VASP) code⁵¹ is adopted to calculate the FeX_3 ML. Generalized gradient approximation (GGA) is used in the scheme of Perdew–Burke–Ernzerhof (PBE).⁵² The strong-correlated correction to the Fe 3d electrons is dealt with the hybrid Heyd–Scuseria–Ernzerhof (HSE06)^{53,54} functional and GGA + U method.⁵⁵ The effective onsite Coulomb interaction parameter (U) and exchange interaction parameter (J_0) are set to be 6.00 and 0.50 eV, respectively. The effective U_{eff} ($U_{\text{eff}} = U - J_0$) is set as 5.50 eV, adopted in the calculation of magnetocrystalline anisotropy (MCA) energy, phonon spectra, and molecular dynamics simulation. The vacuum space in the z -direction is set as 18 Å, and the kinetic energy cutoff is set as 400 eV. The criteria of energy and force are 10^{-6} eV and $1 \text{ meV}\text{\AA}^{-1}$, respectively. The geometry optimization and energy computation are adopted $9 \times 9 \times 1$ and $15 \times 15 \times 1$ Monkhorst–Pack k -grids, respectively. There is Fe element in FeX_3 . Hence, the spin-orbital coupling (SOC) is considered. The noncollinear nonself-consistent calculations are performed to evaluate total energies, after the self-consistent ground states are achieved. The MCA energy is calculated with an energy cutoff of 400 eV, and the corresponding energy criterion is 1×10^{-8} eV. The corresponding k -grid is adopted $15 \times 15 \times 1$, without any symmetry constriction. The phonon spectra and density of the states are calculated using the finite displacement method as implemented in Phonopy software.⁵⁶ A $4 \times 4 \times 1$ cell is adopted in the calculation of phonon spectra and density of the state. The corresponding criteria of energy and Hellmann–Feynman force are 10^{-8} eV and $1 \text{ meV}\text{\AA}^{-1}$, respectively. Eight thousand uniform k -points along high-symmetry lines are used to obtain phonon spectra. To confirm structural stability, *ab initio* molecular dynamics (AIMD) simulation is also performed. The constant moles–volume–

temperature ensemble with a Nosé–Hoover thermostat⁵⁷ is adopted at a temperature of 300 K. The time step and total time are 1 fs and 10 ps, respectively. A larger supercell ($2 \times 2 \times 1$ cell) is adopted in the AIMD simulation, to eliminate the effect of the periodic boundary condition with a smaller system size.

3. RESULTS AND DISCUSSION

3.1. Geometry of FeX_3 ML. The geometry of FeX_3 ML is fabricated and confirmed by PSO⁵⁰ based on the crystal structure analysis, shown in Figure 1a–c. The lattice

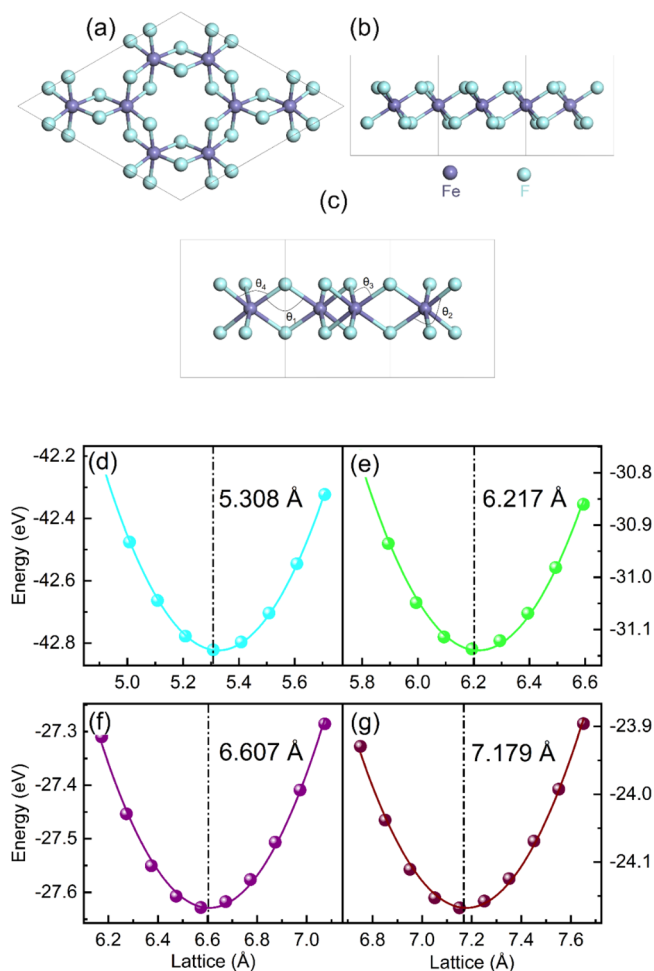


Figure 1. Optimized geometries of (a) top and (b, c) side views of the FeF_3 ML. The medium purple and pale turquoise balls represent Fe and F atoms, respectively. The energies with FM orders of (d) FeF_3 , (e) FeCl_3 , (f) FeBr_3 , and (g) FeI_3 MLs change with lattice parameters.

parameters are obtained from fitting the energy with different strains, shown in Figure 1d–g. The corresponding optimized lattice parameters for FeX_3 ($X = \text{F, Cl, Br, and I}$) are 5.308, 6.217, 6.607, and 7.179 Å (shown in Table 1), which are little larger than the corresponding CrX_3 ($\text{CrF}_3 = 5.200$ Å, $\text{CrCl}_3 = 5.952$ Å, $\text{CrBr}_3 = 6.310$ Å, and $\text{CrI}_3 = 6.842$ Å).⁵⁸ The corresponding Fe-X ($X = \text{F, Cl, Br, and I}$) bond is 1.971, 2.412, 2.579, and 2.798 Å, which is little larger than that of CrX_3 ($X = \text{F, Cl, Br, and I}$) of 1.950, 2.336, 2.492, and 2.705 Å, respectively.⁵⁸ As the atomic number increases, the halogen atomic radius also increases from 71 (F), 99 (Cl), to 114 (Br), and 133 pm (I), respectively. As a result, the corresponding

Table 1. Calculated Lattice Constants a_0 , Total Energy E_t , Bond Angles θ_1 ($\angle\text{Fe-X-Fe}$), Axial Bond Angles θ_2 ($\angle\text{X-Fe-X}$), θ_3 ($\angle\text{X-Fe-X}$), θ_4 ($\angle\text{X-Fe-X}$), and Bond Length l for the FM Order of FeX_3 ($X = \text{F, Cl, Br, I}$)

system	a_0 (Å)	E_t (eV)	θ_1 (deg)	θ_2 (deg)	θ_3 (deg)	θ_4 (deg)	l (Å)
FeF_3	5.308	-300.99	102.1	167.5	93.7	77.9	1.971
FeCl_3	6.217	-234.87	96.0	171.7	90.4	84.0	2.412
FeBr_3	6.607	-212.72	95.2	172.5	90.1	84.8	2.579
FeI_3	7.179	-190.17	95.6	172.1	90.3	84.4	2.798

lattice parameter increases. More details could be found in Table 1.

3.2. Magnetic Properties. The magnetic properties of FeX_3 are also investigated, and the magnetic moment mainly localizes at Fe atoms. Each Fe atom contributes $4.0 \mu_B$ magnetic moment, for all FeX_3 ($X = \text{F, Cl, Br, and I}$). There are eight Fe atoms in the $2 \times 2 \times 1$ cell. There is $32.0 \mu_B$ magnetic moment for the FM order in the supercell. There are four different AFM orders, including AFM-Néel (AFM-N), AFM-stripy (AFM-ST), AFM-zigzag (AFM-ZZ), and AFM-Néel-stripy (AFM-N-ST) orders investigated in this work. For the considered AFM orders, four Fe atoms contribute $16.0 \mu_B$, while the other four Fe atoms contribute $-16.0 \mu_B$ magnetic moment. Therefore, the total magnetic moment equals to $0 \mu_B$. Each of the Fe atoms in FeX_3 ($X = \text{F, Cl, Br, and I}$) with FM orders has a magnetic moment of 4.35, 4.10, 4.01, and $3.88 \mu_B$, respectively. This originates from the different charge transfer from Fe to X atoms. There is 2.06, 1.61, 1.41, and $1.15 e$ electron transfer from the Fe atom to F, Cl, Br, and I atoms, respectively. The corresponding X ($X = \text{F, Cl, Br, and I}$) atoms get 0.68, 0.54, 0.47, and 0.38 e electrons (calculated by the HSE06 functional) with the Bader analysis.⁵⁹ As the atomic number increases, the electronegativity also weakens. Hence, the Fe atoms lose fewer electrons from F, Cl to Br, I. The FeF_3 ML is taken as an example to present magnetic properties of FeX_3 . The spin charge densities with different magnetic orders are shown in Figure 2a–e. The energy difference between FM and AFM orders is defined as $\Delta E = E_{\text{AFM}} - E_{\text{FM}}$. The smallest ΔE corresponding to the energy difference between AFM-ZZ and FM orders ($\Delta E_{\text{AFM-ZZ}} = E_{\text{AFM-ZZ}} - E_{\text{FM}}$) is 0.011, 0.138, 0.023, and 0.028 eV for FeX_3 ($X = \text{F, Cl, Br, and I}$), shown in Table 2. The energy difference between FM and other AFM-N orders defined as $\Delta E_{\text{AFM-N}} (\Delta E_{\text{AFM-N}} = E_{\text{AFM-N}} - E_{\text{FM}})$ is 0.047, 0.223, 0.138, and 0.175 eV, respectively. $\Delta E_{\text{AFM-ST}} (\Delta E_{\text{AFM-ST}} = E_{\text{AFM-ST}} - E_{\text{FM}})$ is 0.036, 0.177, 0.075, and 0.093 eV, respectively. $\Delta E_{\text{AFM-N-S}} (\Delta E_{\text{AFM-N-S}} = E_{\text{AFM-N-S}} - E_{\text{FM}})$ is 0.034, 0.178, 0.077, and 0.097 eV, respectively. The AFM-N order has the highest energy in the considering AFM orders, while the AFM-ZZ order has the lowest energy in the AFM orders (shown in Table 2). Other orders such as noncollinear AFM orders have also been considered, but their energies are higher than the FM orders. The noncollinear AFM order results in the Dzyaloshinskii–Moriya interaction. In a word, all FeX_3 ($X = \text{F, Cl, Br, and I}$) MLs are intrinsic FM materials.

Why does FeX_3 present a FM order? Each Fe atom is coordinated by six ligands-X in FeX_3 , shown in Figure S1. The X–Fe–X bonding angle ($93.7, 90.4, 90.1, \text{ and } 90.3^\circ$) is close to 90° (shown in Table 1), which results in FM coupling according to the Goodenough–Kanamori–Anderson^{60–62} rules of the superexchange theorem. However, there is AFM coupling, which originates from direct Fe–Fe exchange interaction. The ground state is determined by the competition between FM and AFM interaction, similar to the CrI_3 ML.³⁹

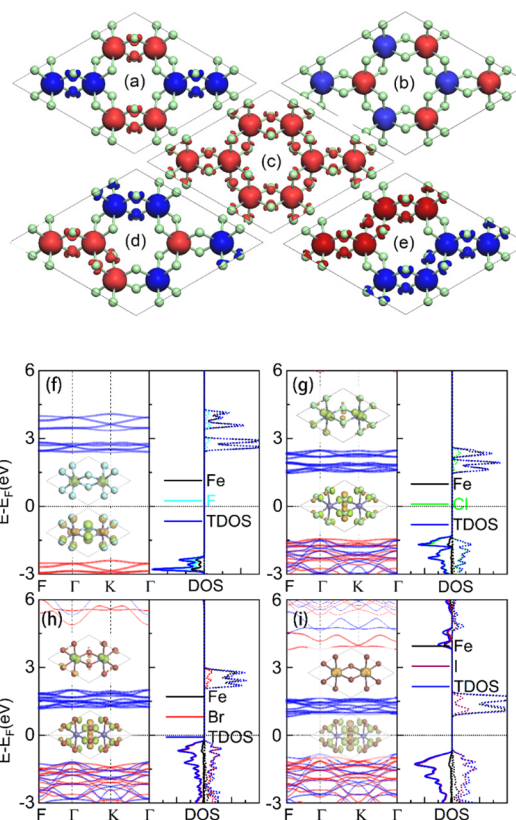


Figure 2. (a–e) Spin charge densities of (a) AFM-ST, (b) AFM-N, (c) FM, (d) AFM-N-ST, and (e) AFM-ZZ orders of FeF_3 . The isovalues is $0.06 e/\text{Å}^3$. The red and blue colors represent spin- α and spin- β electrons, respectively. The spin-polarized band structure and partial density of states (PDOS) of (f) FeF_3 , (g) FeCl_3 , (h) FeBr_3 , and (i) FeI_3 MLs, respectively. The solid and dashed lines represent projected density of states of spin- α and spin- β electrons, respectively. The insets are charge densities of the VBM and CBM, respectively. The isovalues is set $0.6 e/\text{Å}^3$, respectively.

The superexchange interaction in FeX_3 is stronger than Fe–Fe direct exchange interaction. Therefore, all FeX_3 ($X = \text{F, Cl, Br, and I}$) show an FM ground state.

3.3. Electronic Structure. The electronic properties are systematically investigated in this part, and the band structure and density of the state are shown in Figure 2f–i. For FeF_3 and FeCl_3 , the valence band maximum (VBM) is contributed by the spin- α electrons, while the conduction band minimum (CBM) is contributed by the spin- β electrons. Therefore, FeF_3 and FeCl_3 are BMSs. There are three important defined parameters: ΔE_1 , ΔE_2 , and ΔE_3 to describe BMSs, following the routines.^{3,11} The value of ΔE_1 , ΔE_2 , and ΔE_3 is 4.78, 3.84, 0.77 eV and 2.92, 4.46, and 0.12 eV for FeF_3 and FeCl_3 , respectively. More details could be found in Figure S2a,b, in the Supporting Information. However, the VBM and CBM are contributed by spin- β electrons of FeBr_3 and FeI_3 , which

Table 2. Energy Difference (meV) between AFM and FM Orders, Magnetic Moment of Fe Atoms (μ_B), Exchange Parameter, and Curie Temperature Are Listed

SYS	$\Delta E_{\text{AFM-ST}}$	$\Delta E_{\text{AFM-N}}$	$\Delta E_{\text{AFM-N-S}}$	$\Delta E_{\text{AFM-ZZ}}$	MM	J (meV)	T_c (K)
FeF ₃	36	47	34	11	4.35	1.38	56
FeCl ₃	177	223	178	138	4.10	17.25	716
FeBr ₃	75	138	77	23	4.01	2.88	116
FeI ₃	93	176	97	29	3.88	3.63	148

implies that they are HSCs. Moreover, both the VBM and CBM occupied by the spin- β electrons are located at the Γ point of the first Brillouin zone (BZ) of FeF₃. The VBM is located at the Γ point, while the CBM contributed by the spin- β electrons is located at the F point of the first BZ. Therefore, FeCl₃, FeBr₃, and FeI₃ MLs are SCs with indirect band gaps of 2.92, 2.36, and 1.68 eV calculated by the HSE06 functional, respectively, shown in Table 3.

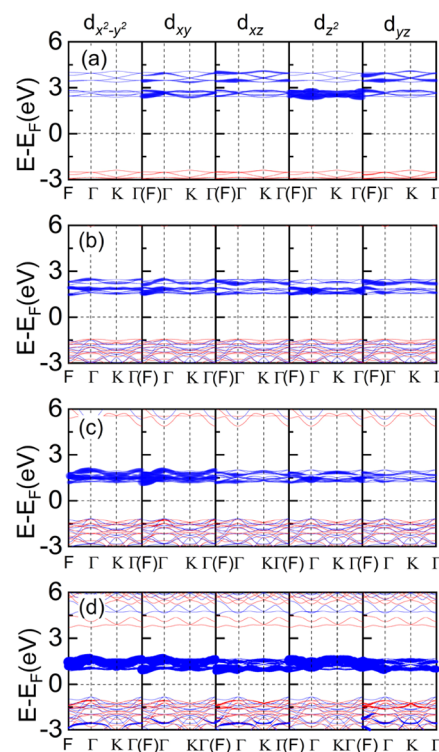
Table 3. Calculated Electronic Property, Band Gap, MAE, and Easy Magnetization Axis Are Listed^a

SYS	Sc	gap (eV)	direct/indirect	MAE (meV/cell)	EA	magnets
FeF ₃	BMS	4.78	D	0.08	<i>c</i>	Ising
FeCl ₃	BMS	2.92	I	0.11	<i>c</i>	Ising
FeBr ₃	HSC	2.36	I	0.59	<i>c</i>	Ising
FeI ₃	HSC	1.69	I	3.19	<i>c</i>	Ising

^aThe MAE is calculated with SOC.

As HSCs, the gaps of spin- α ($E_{g-\alpha}$) and spin- β ($E_{g-\beta}$) channels are usually different from each other. The spin- α electrons' gaps are 7.38, 6.13, and 4.78 eV, while the spin- β electrons' gaps are 2.98, 2.36, and 1.69 eV, for FeCl₃, FeBr₃, and FeI₃, respectively. Hence, spin- β electrons are more easily excited from the VB to the CB, compared with spin- α electrons. The VBM is mainly composed of X's p_x and p_y atomic orbitals, shown in Figure 2 and Figure S3a–f. However, the CBM is mainly contributed by the Fe's d_z^2 (FeF₃) and d_{xz} atomic orbitals (FeCl₃, FeBr₃, and FeI₃), shown in Figure 3a–d and Figure S4a,b, respectively. The charge density of the VBM and CBM also confirms this conclusion. Moreover, the states above the Fermi level are composed of d_z^2 , d_{yz} , d_{xz} , d_{xy} , and $d_{x^2-y^2}$ atomic orbitals of Fe atoms, shown in Figure 3a–d. For FeF₃, the states above the Fermi level are mainly contributed by d_z^2 , d_{yz} , d_{xz} , and d_{xy} atomic orbitals of Fe atoms. However, the states above the Fermi level are contributed by d_z^2 , d_{yz} , d_{xz} , d_{xy} , and $d_{x^2-y^2}$ atomic orbitals of Fe atoms for other FeX₃. Different occupation of the d-orbital affects the different electronic properties of FeX₃ (X = F, Cl, Br, and I),³⁷ which originates from different negativity of X atoms in FeX₃. The LDA functional also confirms above the conclusion, and the corresponding band structures of FeCl₃ and FeBr₃ MLs are shown in Figure S5a,b, respectively.

The band structures of FeX₃ with AFM orders are also calculated, and they are all spin-unpolarized SCs. The corresponding band structure of FeI₃ is shown in Figure S6a–d, in the Supporting Information. The FeI₃ with AFM-N and AFM-ZZ orders is a SC with direct gaps of 1.90 and 1.88 eV, while FeI₃ with AFM-N-ST and AFM-ST orders is a SC with an indirect gap of 1.92 eV. Other FeX₃ show a similar phenomenon. Hence, the orders of magnetic materials are related to the electronic properties.

**Figure 3.** d-Orbital projected band structure of (a) FeF₃, (b) FeCl₃, (c) FeBr₃, and (d) FeI₃ MLs. The first, second, third, fourth, and fifth columns represent $d_{x^2-y^2}$, d_{xy} , d_{xz} , d_z^2 , and d_{yz} orbitals, respectively.

There are Fe atoms in FeX₃. Therefore, the effect of SOC on the electronic properties of FeX₃ is also considered. The corresponding band structures with SOC with EA along [001] and [100] are calculated, shown in Figure S7a–h. Both the VBM and CBM of FeF₃ are located at the K point. Therefore, FeF₃ is still a SC with a direct gap of 4.78 eV. For FeCl₃, FeBr₃, and FeI₃, the VBMs are located at the Γ point, while the CBMs are located at the F point, shown in Figure S7c–h. Hence, they are SCs with indirect band gaps of 2.91, 2.17, and 1.30 eV, respectively. For the heavier element, such as Br and I, there is an obvious energy-splitting at the K point, shown in Figure S7e–h. More details could be found in the Supporting Information. However, there is a difference between band structures without SOC and with SOC, when the atomic mass increases.

3.4. Curie Temperature. The FM materials with high Curie temperature (T_c) are highly desirable. It is expected that T_c is large enough in the application. The classic Ising model is used to evaluate J and T_c . The magnetic configurations are shown in Figure 4a,b, and we assume the interactions nearest-neighbor only. The Hamiltonian can be written as:

$$H = -J \sum_{\langle i,j \rangle} S_i \times S_j \quad (1)$$

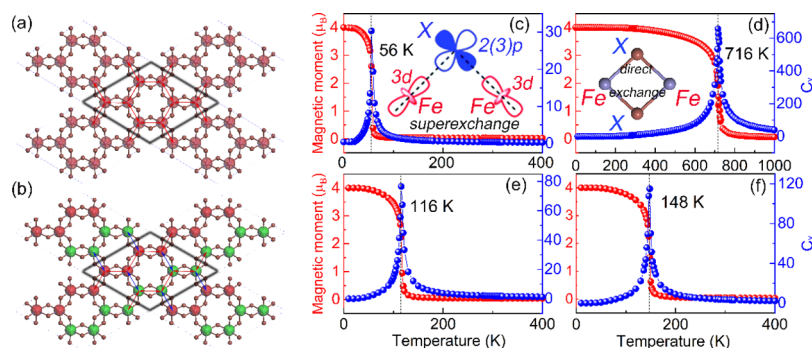


Figure 4. (a and b) Ising model considering the nearest exchange interactions. The spin densities of (a) FM and (b) AFM-ZZ orders of FeX_3 ($X = \text{F, Cl, Br, and I}$). The red and green colors present spin- α and spin- β electron spin densities, respectively. The red and blue arrows present Fe atoms ferromagnetically and antiferromagnetically couple with the nearest Fe atoms, respectively. The black diamond presents an adopted supercell in the simulation. (c–f) Magnetic moment per unit cell (red) and specific heat (C_v) (blue) of (c) FeF_3 , (d) FeCl_3 , (e) FeBr_3 , and (f) FeI_3 vary with respect to the temperature from classic Ising model Monte Carlo (MC) simulation, respectively. The inset of (c) and (d) is the mechanism of superexchange interaction for a 90° bond angle and direct exchange interaction, respectively.

$$E_{\text{FM}} = E_0 - \left(\frac{1}{2} \times 8 \times 3\right) J |S|^2 \quad (2)$$

$$E_{\text{AFM-ZZ}} = E_0 - 8 \times \left(-\frac{1}{2} \times 1 + \frac{1}{2} \times 1 \times 2\right) J |S|^2 \quad (3)$$

$$J = \frac{E_{\text{AFM-ZZ}} - E_{\text{FM}}}{8 |S|^2} \quad (4)$$

where E_{FM} and $E_{\text{AFM-ZZ}}$ represent energies of FM and AFM-ZZ ($E_{\text{AFM-ZZ}} < E_{\text{AFM-ST}} < E_{\text{AFM-N-ST}} < E_{\text{AFM-N}}$ for FeCl_3 , FeBr_3 , and FeI_3) orders, respectively. J and H are the exchange parameter and Hamilton, respectively, and S_i represents the spin operator. Each Fe atom has $4.0 \mu_B$ magnetic moment. The energies of FM and AFM (AFM-ZZ) orders could be evaluated with eqs 2 and 3, respectively. The exchange parameter is calculated with eq 4, and J is equal to 1.38, 17.25, 2.88, and 3.63 meV for FeX_3 ($X = \text{F, Cl, Br, and I}$), shown in Table 2. The mean field theory usually overestimates T_c .⁶³ Therefore, we use classic Heisenberg model Monte Carlo (MC) simulation to evaluate T_c by calculating the magnetic moment as a function of temperature. This MC code is developed by Prof. Hongjun Xiang.⁶⁴ As a benchmark, the T_c of CrI_3 is evaluated to be 51 K with this method, which agrees well with the experimental value of 45 K.⁷ A larger 90×90 cell with 1.0×10^7 loops is used in the T_c calculation. The simulation with larger cells with more loops gives a similar result. The $4.0 \mu_B$ magnetic moment per Fe atom drops quickly, and the paramagnetic orders are achieved at a temperature of 80, 840, 160, and 200 K for FeF_3 , FeCl_3 , FeBr_3 , and FeI_3 , respectively. The corresponding T_c values are predicted to be 56, 716, 116, and 148 K, respectively. The T_c of FeX_3 ($X = \text{F, Cl, Br, and I}$) is higher than that of CrCl_3 (12.1 K⁶⁵ and 29.7 K⁶⁵), CrBr_3 (23.1 K⁶⁵ and 41.3 K⁴⁹), and CrI_3 (42.2 K⁶⁵ and 46.4 K⁴⁹).

3.5. Magnetocrystalline Anisotropy. For magnetic materials, when a magnetic moment is switched from EA to hard axis, it needs energy.³⁸ This energy named MAE is to overcome the “barrier.”³⁷ MCA is MAE per unit area. The FM materials with high MAE (MCA) are expected in spintronics.

For systems with high symmetry, the energy at certain direction (θ, ϕ) follows the following equation:⁶⁶

$$\Delta E_0 = K_1 \cos^2 \theta + K_2 \cos^4 \theta + K_3 \cos 3\phi \quad (5)$$

$$\Delta E_0 = E - E_0 \quad (6)$$

where E represents energy in a certain direction (θ, ϕ) with the polar angle θ and azimuthal angle ϕ . E_0 presents the global energy minimum. K_1 and K_2 represent quadratic and quartic contribution to the MAE, respectively. The energy difference ΔE_0 is independent of the in-plane azimuthal angle ϕ ,⁶⁷ which implies $K_3 = 0$. More details are shown in Figure 5a–d. This point could be also concluded from the symmetry (FeX_3 has the D_{3d} space group). Therefore, eq 5 is simplified into the equation:

$$\Delta E_0 = K_1 \cos^2 \theta + K_2 \cos^4 \theta \quad (7)$$

ΔE_0 equals 0 eV, when θ equals $\frac{\pi}{2}$. However, E_0 reaches the maximum, as θ equals to 0. It indicates that EA prefers to be PMA (along the [001] direction). The energy difference (ΔE_0) changes as a function of polar angle θ , shown in Figure 5a–d. However, the ΔE_0 is related to U_{eff} as MCA originates from SOC. When the effect of SOC is described by the GGA + U method, the evaluated value is affected by U_{eff} and more details could be found in Figure S8 and S9a,b. We have tested MCAs with different U_{eff} s and found that MAE and MCA are affected by U_{eff} . When U_{eff} equals to 5.5 eV, ΔE_0 (with meV unit) follows the equation: $\Delta E_0 = 0.0821 \cos^2 \theta + 0.00002 \cos^4 \theta$ (FeF_3) and $\Delta E_0 = 0.1155 \cos^2 \theta + 0.000154 \cos^4 \theta$ (FeCl_3). The corresponding equations are shown as follows: $\Delta E_0 = 0.6002 \cos^2 \theta - 0.0004 \cos^4 \theta$ (FeBr_3) and $\Delta E_0 = 2.680 \cos^2 \theta + 0.523 \cos^4 \theta$ (FeI_3). Therefore, the MAE and MCA could be evaluated with the following formulas:

$$\text{MAE} = E_{[100]} - E_{[001]} \quad (8)$$

$$\text{MCA} = E_{[100]} - E_{[001]} = \text{MAE}/S \quad (9)$$

$$S = a^2 \sin \frac{\pi}{3} \quad (10)$$

$E_{[100]}$ and $E_{[001]}$ represent total energies with the magnetic axis along [100] and [001] directions, respectively. S is the area of the supercell. When MAE and MCA are negative, it indicates an in-plane preference for magnetization (IMA). In contrast, the positive MAE (MCA) means that it intends PMA. The MAE of 2D materials is larger than that of three-dimensional materials for reduced dimensionality. FeX_3 are 2D materials, which is expected to have a sizable MCA. The MAE (MCA) of

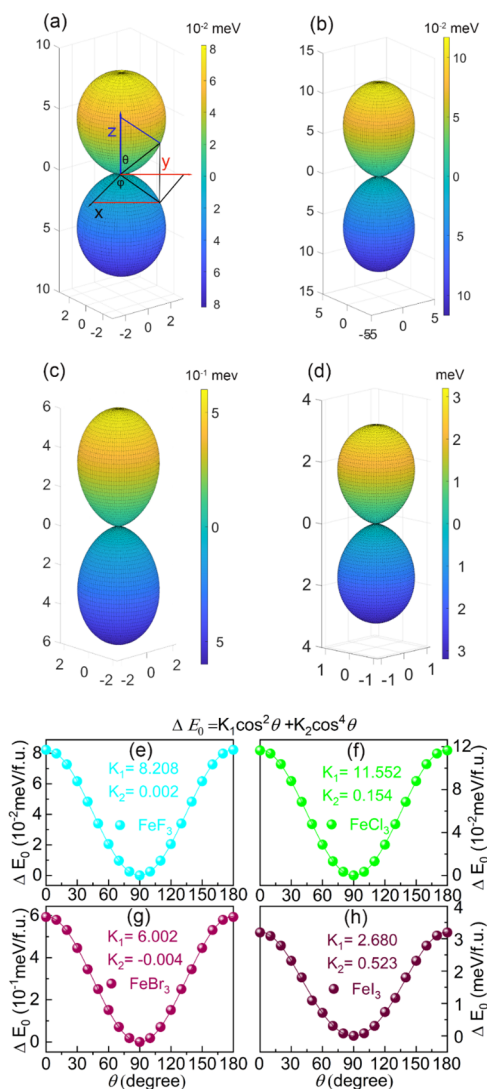


Figure 5. MAE varies as a function of polar angle θ and φ for (a, e) FeF_3 , (b, f) FeCl_3 , (c, g) FeBr_3 , and (d, h) FeI_3 ML. The MAE is calculated with the GGA + U method.

FeX_3 ($X = \text{F, Cl, Br, and I}$) MLs is 0.08 (MCA = 0.005 erg/cm²), 0.11 (0.055 erg/cm²), 0.59 (0.252 erg/cm²), and 3.19 (1.145 erg/cm²) meV when the U_{eff} equals to 5.5 eV (shown in Table 3). The FeX_3 shows positive MAE, which means that FeX_3 is an Ising magnet, shown in Table 3. MAEs are larger than that of CrBr_3 (0.16 meV)^{49,68} and CrI_3 (0.80 meV).^{7,49} These values are larger than those of the most known 2D magnets.^{69,70} Why FeX_3 prefer PMA? It originates from the indirect SOC between Fe and X atoms, and a similar phenomenon also appears in CrI_3 .⁷¹ Moreover, the strength of the indirect SOC also enhances as the halogen atomic number increases.⁷¹ Therefore, the MAE (MCA) increases from F, Cl to Br, I atoms. Moreover, FeX_3 ($X = \text{F, Cl, Br, and I}$) are Ising magnets, shown in Table 3.

The work function of FeX_3 is also evaluated by calculating xy -averaged electrostatic potential. The corresponding work functions are 6.99 (FeF_3), 8.47 (FeCl_3), 7.42 (FeBr_3), and 6.28 eV (FeI_3), which implies that electrons need different energies to excite from the VBM to the vacuum energy level. The corresponding xy -averaged electrostatic potential is shown in Figure S10a–d.

3.6. Dynamical and Thermal Stability. The dynamical stability of FeX_3 is confirmed via phonon dispersion curves and phonon density of the states, which show no obvious imaginary phonon modes. The highest vibration frequency is 12.19 ($X = \text{F}$), 9.35 (Cl), 7.01 (Br), and 5.81 (I) THZ, which is lower than that of CrF_3 (17.99 THZ), CrCl_3 (10.94 THZ), CrBr_3 (9.05 THZ), and CrI_3 (7.32 THZ), shown in Figure S11a–h, Supporting Information. It can be found that the contribution mainly comes from X atoms for the low frequency ($0 < \epsilon < 3.5$ THZ), shown in Figure 6a–d. On the contrary, Fe atoms do

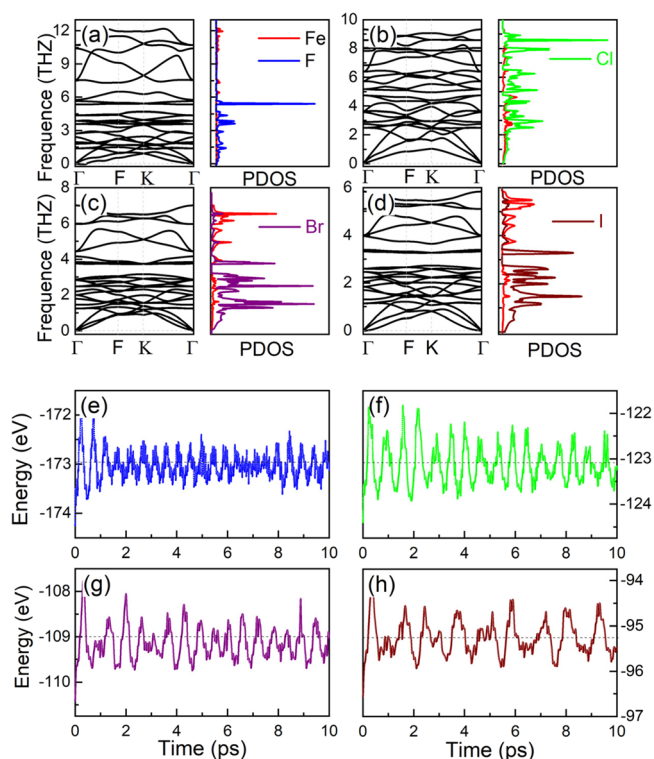


Figure 6. (a–d) Phonon spectrum density of the state of (a) FeF_3 , (b) FeCl_3 , (c) FeBr_3 , and (d) FeI_3 ML. The red, blue, green, purple, and dark wine red lines represent Fe, F, Cl, Br, and I atoms' projected phonon DOS, respectively. (e–h) AIMD of the evaluation of energy at the PBE + U level for 10 ps at 300 K. The blue, green, purple, and wine red lines represent total energies of (e) FeF_3 , (f) FeCl_3 , (g) FeBr_3 , and (h) FeI_3 , respectively, and 0.018 eV per atom, respectively. The snapshots of the geometries, shown in Figure S12a–d, also confirm the intact structures. No obvious structure distortion is found, and FeX_3 is expected to be stabilized at room temperature. It is sure that the geometries of FeX_3 are stable at room temperature.

the main contribution in the high-frequency ($3.5 < \epsilon < 5.8$ THZ) zone. As a result, this affects the heat transfer properties. Compared with X (F, Cl, Br, and I) atoms (atomic weight: 19.0, 35.5, 79.9, and 126.9), the Fe atom (55.85) is lighter. Therefore, the Fe atom makes main contribution to the phonon with high energy, while X atoms make contribution to the phonon with low energy, shown in Figure 6a–d. At low temperature, the thermal conductivity is mainly contributed by X atoms with low-frequency phonons. However, the thermal conductivity is mainly contributed by the phonon with high frequency (Fe atom), at high temperature. Why the highest vibration frequency of CrX_3 (F, Cl, Br, I) is higher than that of FeX_3 ? There are two reasons: (1) The vibration mode with higher frequency in MX_3 is contributed by metal atoms. (2) Cr

atoms (atomic weight: 52) are little lighter than Fe atoms (atomic weight: 55.85).

The thermal stability of FeX_3 is evaluated with AIMD, which is widely used to research the stability of materials. To examine whether FeX_3 is stable, we perform AIMD simulations at 300 K. The fluctuations in the total energies are shown in Figure 6e–h. The total energies of FeX_3 ($X = \text{F}, \text{Cl}, \text{Br}, \text{and I}$) vibrate round -172.96 eV ($X = \text{F}$), -122.09 eV (Cl), -109.00 eV (Br), and -95.26 eV (I) at 300 K, with the amplitude about 0.013, 0.011, and 0.015.

3.7. Carriers Modulate FeX_3 ($X = \text{Cl}$ and I). In general, these synthesized 2D MLs are usually positively or negatively charged.¹¹ Moreover, carrier doping is a common method to effectively control the magnetic and electronic properties of 2D materials.^{11,72} Therefore, it is necessary to explore the carrier's doping effect on the properties of the FeX_3 ML. The VBM and CBM of BMS materials are contributed by different spin electrons.^{3,11} A little injected electrons (or holes) would only occupy the conduction band in one channel (or the valence band in another channel).^{3,11} Therefore, charge doping could drive a BMS-to-HM electronic phase transition.^{3,11,73} Moreover, HM can provide 100% spin-polarized carriers, which has wide applications in electronics.^{3,11,37,73–75} Previous studies have shown that it is likely to induce magnetic transition by carrier doping.^{3,11,73} The carrier doping could introduce unpaired p or d electrons.^{3,11,75} As a result, carrier doping is expected to manipulate the electromagnetic properties of the FeX_3 ML.

The charge doping could introduce magnetic phase transformation between FM and Ferrim orders in FeX_3 . The carrier doping affects magnetic moments by introducing additional electrons or holes into the supercell.¹¹ Taking FeCl_3 with a $2 \times 2 \times 1$ cell as an example, it has $40 \mu_B$ magnetic moment, and corresponding results are shown in Figure 7a. It is interesting that doping either n electrons or holes will reduce the magnetic moment with $n \mu_B$, as $|n| < 0.39 e$. ΔE is defined as the following equation: $\Delta E = E_{\text{FM}} - E_{\text{Ferrim-ZZ}}$, which is used to describe the energy difference between FM and Ferrim orders. The $E_{\text{Ferrim-ZZ}}$ presents the total energy of the ferrimagnetic-zigzag (Ferrim-ZZ) order, which is similar to the AFM-ZZ order, shown in the inset of Figure 7a. When the negative carriers are doped, the ΔE s are 0.113 eV ($-0.3 e$) and 0.005 eV ($-0.37 e$), respectively. As more negative charges are doped, the corresponding ΔE becomes smaller, shown in Figure 7a. When the negative carriers are further introduced, the direct exchange interaction between Fe atoms is further weakened. As the negatively doped charge is $-0.39 e$, the corresponding ΔE is -0.003 eV. Hence, there is a magnetic order transformation from FM to Ferrim orders at a critical carrier doping of $-0.39 e$. The FeCl_3 ML has $|n| \mu_B$ magnetic moment. As more negative charges are further doped, ΔE are decreased to -0.221 eV ($-0.6 e$) and -0.327 eV ($-0.9 e$), respectively.

When the positive carriers are doped, the ΔE is first increased to 0.138 ($+0.1 e$), 0.139 ($+0.2 e$), 0.140 ($+0.3 e$), and 0.141 ($+0.4 e$) eV, respectively. When the q is large than $0.45 e$, ΔE is monotonously decreased to 0.127 ($+0.6 e$), 0.069 ($+0.9 e$), and 0.032 eV ($+1.2 e$), respectively. As more positive carriers are doped, the ΔE decreases as the positive charge could suppress the super exchange interaction between Fe and Cl atoms. However, the ΔE is positive, which implies that FeCl_3 still shows a robust FM ordered ground state over a wide range.

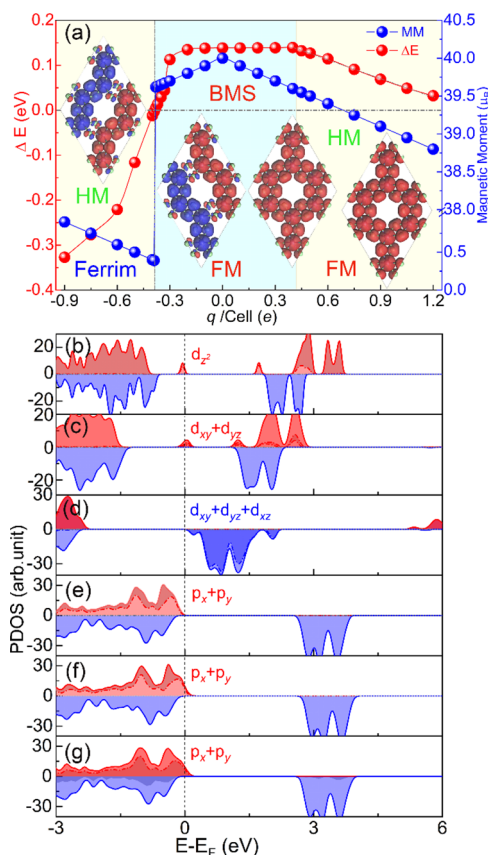


Figure 7. Electron and hole dope the FeCl_3 ML. (a) ΔE , electronic properties, magnetic moment, and order change with doped charges. The PDOS change with doped charges of (b) -0.9 , (c) -0.6 , (d) -0.3 , (e) 0.3 , (f) 0.6 , and (g) $1.2 e$, respectively. The shadow parts represent the contribution from d or p-orbitals. The insets are spin charge densities of FeCl_3 doped with -0.9 and $0.6 e$ charge, respectively. The isovalue is set at $0.03 e/\text{\AA}^3$. The yellow and blue areas in the inset of (a) represent the HM and BMS, respectively.

The electronic properties are closely related to the magnetic orders, shown in Figure 7b–g and Figure S13a–h. The FeCl_3 ML represents a BMS without charge doping. When the negative carrier is doped with $-0.2 e$, the original VBM is contributed by spin- β electrons, while the CBM is contributed by the d (d_{xy} , d_{yz} , d_{xz}) orbital of spin- β electrons, shown in Figure 7d. Therefore, the FeCl_3 is still a BMS. As $-0.6 e$ electrons are introduced, the spin- α electrons would partially occupy d_{xy} and d_{yz} orbitals, shown in Figure 7c. The FeCl_3 is transformed into a HM. In a word, the negative carriers would modulate FeCl_3 from the BMS with FM orders to BMS (FM or Ferrim orders) ($|q| < 0.39 e$) or HM (Ferrim or FM orders) ($|q| > 0.39 e$), shown in Figure S13a–d. When the positive charge is introduced, it means that part of electrons will be “pumped” from the VBM of FeCl_3 . The states at the Fermi level are mainly contributed by spin- α electrons’ p_x and p_y orbitals, shown in Figure 7e–g. When the less hole ($q < 0.45 e$) is introduced, FeCl_3 is still a BMS with an FM order, shown in Figure 7e and Figure S13e–h.

As more holes are doped, the states at the Fermi level also increase, shown in Figure 7f,g and Figure S13g,h. The spin- α electrons intend to partially occupy the Fermi level, while the spin- β electron channel shows insulating properties. Therefore, the positively charged ($q > 0.45 e$) FeCl_3 is transformed into a HM, whose spin- α electron is insulating, shown in Figure

S13g,h. In a word, the carrier could modulate magnetic and electronic properties by changing the super exchange interaction between Fe and Cl atoms or direct exchange interaction between Fe atoms, shown in Figure 7a. As a result, the FeCl₃ could be tuned from the BMS (FM order) to BMS (FM or Ferrim orders) or HM (FM or Ferrim orders), depending on the charge magnitude. More details could be found in Figure S13ah, in the Supporting Information.

As FeI₃ is doped with the carriers, the corresponding magnetic moment and ΔE also change with the charge, shown in Figure 8a. The original FeI₃ is a HSC with an intrinsic FM

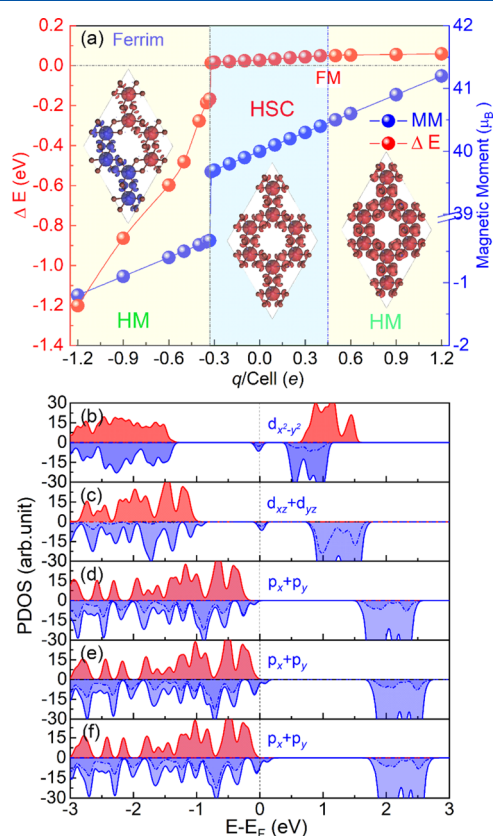


Figure 8. Electron and hole doped FeI₃ ML. (a) ΔE , electronic properties, magnetic moment, and order change with doped carriers. The PDOS changes with doped charges of (b) -1.2 , (c) -0.6 , (d) -0.3 , (e) $+0.6$, and (f) $+0.9$ e , respectively. The shadow parts represent the contribution from d or p-orbitals. The insets are spin charge densities of -0.6 , $+0.3$, and $+0.6$ e carrier doped FeI₃. The isovalue is set to 0.04 $e/\text{\AA}^3$.

order. In the previous work, the HSC could be easily transformed into HM with charge's doping.^{3,11} Moreover, the FeI₃ is changed from the FM order into Ferrim order with negative charge's doping ($|q| > 0.33$ e). The corresponding magnetic moment equals to $|q| \mu_B$. As the positive charges are doped in FeI₃, the magnetic moment equals to $42 - |q| \mu_B$. The corresponding ΔE is also increased, as the positive charge increases. When -0.1 , -0.2 , and -0.3 e electrons are doped in FeI₃, the corresponding ΔE is 0.024 , 0.020 , and 0.017 eV , respectively. It implies that FeI₃ still shows an FM order, as less negative charge ($|q| < 0.33$ e) is doped in FeI₃. The corresponding magnetic moment equals to $42 - |q| \mu_B$, shown in Figure 8a. As more electrons ($q = -0.33$ e) are doped, the ΔE s become negative, implying that FeI₃ is converted from FM to Ferrim orders (the corresponding net

magnetic moment is not zero), shown in Figure 8a. The corresponding ΔE is -0.277 (-0.4 e), -0.598 (-0.6 e), -0.864 (-0.9 e), and -1.201 eV (-1.2 e), respectively. As more electrons are "injected" into FeI₃, the Fermi level is also increased. The VBs contributed by d-orbitals (d_{xz} , d_{yz} , and $d_{x^2-y^2}$ orbitals) are partially occupied by spin- β electrons, while the spin- α electron channel is insulating, shown in Figure 8b,c. Therefore, FeI₃ is a HM. The corresponding magnetic moment monotonously increases as more electrons are injected into FeI₃.

When the positive carriers are injected into FeI₃, the ΔE is 0.041 ($+0.3$ e), 0.053 ($+0.6$ e), 0.056 ($+0.9$ e), and 0.059 ($+1.2$ e) eV , respectively. The ΔE monotonously increases, implying enhancement of the superexchange interaction between Fe and I atoms. The states near the Fermi level are mainly contributed by p_x and p_y orbitals, shown in Figure 8d-f. As more electrons are "pumped away," the Fermi level is partially occupied by the spin- β electrons. As a result, the FeI₃ is transformed from HSC to HM, and the states at the Fermi level are also increased, shown in Figure 8e,f. Moreover, a charge density injection $\sim 10^{15}$ cm^{-2} has been experimentally achieved in low-dimensional systems using an ionic liquid as a gate dielectric.⁷⁶ Hence, the controllable carrier doping would be realized using available gating techniques.

4. CONCLUSIONS

In summary, we have predicted and investigated magnetic and electronic properties of FeX₃ ($X = \text{F, Cl, Br, and I}$) MLs. We have found intrinsic ferromagnetism in FeX₃ MLs using particle-swarm search approaches and first-principles. All FeX₃ show an intrinsic FM order, and the ferromagnetism comes from the superexchange interaction of Fe-X-Fe bonds with angle close to 90° . FeX₃ ($X = \text{F, Cl, Br, and I}$) have a T_c of 56, 716, 116, and 148 K, respectively. FeF₃ and FeCl₃ are BMSs with (direct) and (indirect) gaps of 4.78 and 2.92 eV , respectively, while FeBr₃ and FeI₃ are HSCs with indirect gaps of 2.36 and 1.69 eV , respectively. The EA of FeX₃ ($X = \text{F, Cl, Br, and I}$) is along the $[001]$ direction, and MAE is 0.08, 0.11, 0.59, and 3.19 meV , respectively. The magnetic and electronic properties of FeX₃ are different, which is attributed to the different Fe d-orbitals' occupation. All FeX₃ show good dynamical and thermal stability. The FeCl₃ and FeI₃ can be transformed from the BMS or HSC (FM order) into HM (FM or Ferrim orders) by carrier doping in a wide range. Our work presents FM FeX₃ MLs with high Curie temperature, high MAE, and tunable electronic properties, implying wide potential application in spin-electronics.

■ ASSOCIATED CONTENT

Supporting Information

The Supporting Information is available free of charge at <https://pubs.acs.org/doi/10.1021/acs.jpcc.1c03915>.

Information on materials, parameters in CALYPSO, band structure of FeF₃ and FeCl₃, p-orbital projected band structure of FeF₃ and FeCl₃, PDOS of FeF₃ and FeI₃, band structure with LDA, band structure with AFM orders, band structure with SOC, U test, MAE test, indirect SOC, work function, phonon spectrum and phonon density of ML CrX₃ ($X = \text{F, Cl, Br, and I}$), snapshots of the atomic structure with AIMD, and band structure of FeCl₃ doped with carriers (PDF)

AUTHOR INFORMATION

Corresponding Author

Zhaoyong Guan – Key Laboratory of Colloid and Interface Chemistry, Ministry of Education, School of Chemistry and Chemical Engineering, Shandong University, Jinan, Shandong 250100, P. R. China; Science Center for Material Creation and Energy Conversion, School of Chemistry and Chemical Engineering, Institute of Frontier and Interdisciplinary Science, Shandong University, Jinan, Shandong 250100, P.R. China; orcid.org/0000-0002-6847-5809; Phone: +86-0531-88363179; Email: zyguan@sdu.edu.cn

Author

Shuang Ni – Research Center of Laser Fusion, China Academy of Engineering Physics, Mianyang, Sichuan 621900, P. R. China

Complete contact information is available at:
<https://pubs.acs.org/10.1021/acs.jpcc.1c03915>

Notes

The authors declare no competing financial interest.

ACKNOWLEDGMENTS

The authors thank Prof. Wenhui Duan and Xingxing Li for discussion of evaluation of Curie temperature, Prof. Liang Ma, Shuqing Zhang, and Chunmei Zhang for calculation of MAE/MCA, Dr. Yizhou Liu for 3D plots of MAE using MATLAB, and Prof. Chengxi Huang and Fawei Zheng for the calculation of the exchange parameter. This work was supported by the financial support from the Natural Science Foundation of China (Grant No. 11904203) and the Fundamental Research Funds of Shandong University (Grant No. 2019GN065). The scientific calculations in this paper have been performed on the HPC Cloud Platform of Shandong University. The authors also acknowledge the Beijing Super Cloud Computing Center (BSCC) and Shanghai Supercomputer Center for providing HPC resources.

REFERENCES

- (1) Geim, A. K.; Novoselov, K. S. The Rise of Graphene. *Nat. Mater.* **2007**, *6*, 183–191.
- (2) Castro Neto, A. H.; Guinea, F.; Peres, N. M. R.; Novoselov, K. S.; Geim, A. K. The Electronic Properties of Graphene. *Rev. Mod. Phys.* **2009**, *81*, 109–162.
- (3) Guan, Z.; Si, C.; Hu, S.; Duan, W. First-Principles Study of Line-Defect-Embedded Zigzag Graphene Nanoribbons: Electronic and Magnetic Properties. *Phys. Chem. Chem. Phys.* **2016**, *18*, 12350–12356.
- (4) Zhang, Y. B.; Tan, Y. W.; Stormer, H. L.; Kim, P. Experimental Observation of the Quantum Hall Effect and Berry's Phase in Graphene. *Nature* **2005**, *438*, 201–204.
- (5) Radisavljevic, B.; Radenovic, A.; Brivio, J.; Giacometti, V.; Kis, A. Single-Layer MoS₂ Transistors. *Nat. Nanotechnol.* **2011**, *6*, 147–150.
- (6) Gong, C.; et al. Discovery of Intrinsic Ferromagnetism in Two-Dimensional Van Der Waals Crystals. *Nature* **2017**, *546*, 265.
- (7) Huang, B.; et al. Layer-Dependent Ferromagnetism in a Van Der Waals Crystal Down to the Monolayer Limit. *Nature* **2017**, *546*, 270.
- (8) Sun, Z.; et al. Giant Nonreciprocal Second-Harmonic Generation from Antiferromagnetic Bilayer CrI₃. *Nature* **2019**, *572*, 497–501.
- (9) McGuire, M. A.; Dixit, H.; Cooper, V. R.; Sales, B. C. Coupling of Crystal Structure and Magnetism in the Layered, Ferromagnetic Insulator CrI₃. *Chem. Mater.* **2015**, *27*, 612–620.
- (10) Golberg, D.; Bando, Y.; Huang, Y.; Terao, T.; Mitome, M.; Tang, C. C.; Zhi, C. Y. Boron Nitride Nanotubes and Nanosheets. *ACS Nano* **2010**, *4*, 2979–2993.
- (11) Guan, Z.; Wang, W.; Huang, J.; Wu, X.; Li, Q.; Yang, J. Tunable Electronic and Magnetic Properties of Graphene Flake-Doped Boron Nitride Nanotubes. *J. Phys. Chem. C* **2014**, *118*, 28616–28624.
- (12) Guan, Z.; Lian, C.-S.; Hu, S.; Ni, S.; Li, J.; Duan, W. Tunable Structural, Electronic, and Optical Properties of Layered Two-Dimensional C₂N and MoS₂ Van Der Waals Heterostructure as Photovoltaic Material. *J. Phys. Chem. C* **2017**, *121*, 3654–3660.
- (13) Guan, Z.; Ni, S.; Hu, S. Tunable Electronic and Optical Properties of Monolayer and Multilayer Janus MoSSe as a Photocatalyst for Solar Water Splitting: A First-Principles Study. *J. Phys. Chem. C* **2018**, *122*, 6209–6216.
- (14) Wang, Q. H.; Kalantar-Zadeh, K.; Kis, A.; Coleman, J. N.; Strano, M. S. Electronics and Optoelectronics of Two-Dimensional Transition Metal Dichalcogenides. *Nat. Nanotechnol.* **2012**, *7*, 699–712.
- (15) Liao, M.; et al. Superconductivity in Few-Layer Stanene. *Nat. Phys.* **2018**, *14*, 344–348.
- (16) Mermin, N. D.; Wagner, H. Absence of Ferromagnetism or Antiferromagnetism in One- or Two-Dimensional Isotropic Heisenberg Models. *Phys. Rev. Lett.* **1966**, *17*, 1133–1136.
- (17) Song, T.; et al. Giant Tunneling Magnetoresistance in Spin-Filter Van Der Waals Heterostructures. *Science* **2018**, *360*, 1214–1218.
- (18) Cai, X.; et al. Atomically Thin CrCl₃: An in-Plane Layered Antiferromagnetic Insulator. *Nano Lett.* **2019**, *19*, 3993–3998.
- (19) Burch, K. S. Electric Switching of Magnetism in 2D. *Nat. Nanotechnol.* **2018**, *13*, 532–532.
- (20) Huang, B.; et al. Electrical Control of 2D Magnetism in Bilayer CrI₃. *Nat. Nanotechnol.* **2018**, *13*, 544–548.
- (21) Ghazaryan, D.; et al. Magnon-Assisted Tunneling in Van Der Waals Heterostructures Based on CrBr₃. *Nature Electronics* **2018**, *1*, 344–349.
- (22) Deng, Y.; et al. Gate-Tunable Room-Temperature Ferromagnetism in Two-Dimensional Fe₃GeTe₂. *Nature* **2018**, *563*, 94–99.
- (23) Gibertini, M.; Koperski, M.; Morpurgo, A. F.; Novoselov, K. S. Magnetic 2D Materials and Heterostructures. *Nat. Nanotechnol.* **2019**, *14*, 408–419.
- (24) Wang, N.; Tang, H.; Shi, M.; Zhang, H.; Zhuo, W.; Liu, D.; Meng, F.; Ma, L.; Ying, J.; Zou, L.; Sun, Z.; Chen, X. Transition from Ferromagnetic Semiconductor to Ferromagnetic Metal with Enhanced Curie Temperature in Cr₂Ge₂Te₆ Via Organic Ion Intercalation. *J. Am. Chem. Soc.* **2019**, *141*, 17166–17173.
- (25) Verzhbitskiy, I. A.; Kurebayashi, H.; Cheng, H.; Zhou, J.; Khan, S.; Feng, Y. P.; Eda, G. Controlling the Magnetic Anisotropy in Cr₂Ge₂Te₆ by Electrostatic Gating. *Nature Electronics* **2020**, *3*, 460–465.
- (26) Bonilla, M.; Kolekar, S.; Ma, Y.; Diaz, H. C.; Kalappattil, V.; Das, R.; Eggers, T.; Gutierrez, H. R.; Manh-Huong, P.; Batzill, M. Strong Room-Temperature Ferromagnetism in VSe₂ Monolayers on Van Der Waals Substrates. *Nat. Nanotechnol.* **2018**, *13*, 289–293.
- (27) Verchenko, V. Y.; Tsirlin, A. A.; Sobolev, A. V.; Presniakov, I. A.; Shevelkov, A. V. Ferromagnetic Order, Strong Magnetocrystalline Anisotropy, and Magnetocaloric Effect in the Layered Telluride Fe_{3-δ}GeTe₂. *Inorg. Chem.* **2015**, *54*, 8598–8607.
- (28) Li, X.; Lu, J.-T.; Zhang, J.; You, L.; Su, Y.; Tsymbal, E. Y. Spin-Dependent Transport in Van Der Waals Magnetic Tunnel Junctions with Fe₃GeTe₂ Electrodes. *Nano Lett.* **2019**, *19*, 5133–5139.
- (29) Yu, W.; Li, J.; Herng, T. S.; Wang, Z.; Zhao, X.; Chi, X.; Fu, W.; Abdelwahab, I.; Zhou, J.; Dan, J.; Chen, Z.; Chen, Z.; Li, Z.; Lu, J.; Pennycook, S. J.; Feng, Y. P.; Ding, J.; Loh, K. P. Chemically Exfoliated VSe₂ Monolayers with Room-Temperature Ferromagnetism. *Adv. Mater.* **2019**, *31*, No. 1903779.
- (30) Zhang, S.; Xu, R.; Luo, N.; Zou, X. Two-Dimensional Magnetic Materials: Structures, Properties and External Controls. *Nanoscale* **2021**, *13*, 1398–1424.

- (31) Li, H.; Ruan, S.; Zeng, Y.-J. Intrinsic Van Der Waals Magnetic Materials from Bulk to the 2D Limit: New Frontiers of Spintronics. *Adv. Mater.* **2019**, *31*, 1900065–1900099.
- (32) Novoselov, K. S.; Mishchenko, A.; Carvalho, A.; Neto, A. H. C. 2D Materials and Van Der Waals Heterostructures. *Science* **2016**, *353*, No. aac9439.
- (33) Niu, B.; et al. Coexistence of Magnetic Orders in Two-Dimensional Magnet CrI₃. *Nano Lett.* **2020**, *20*, 553–558.
- (34) Chen, W.; Sun, Z.; Wang, Z.; Gu, L.; Xu, X.; Wu, S.; Gao, C. Direct Observation of Van Der Waals Stacking-Dependent Interlayer Magnetism. *Science* **2019**, *366*, 983–987.
- (35) Si, C.; Zhou, J.; Sun, Z. Half-Metallic Ferromagnetism and Surface Functionalization-Induced Metal–Insulator Transition in Graphene-Like Two-Dimensional Cr₂C Crystals. *ACS Appl. Mater. Interfaces* **2015**, *7*, 17510–17515.
- (36) Suarez Morell, E.; Leon, A.; Hiroki Miwa, R.; Vargas, P. Control of Magnetism in Bilayer CrI₃ by an External Electric Field. *2D Materials* **2019**, *6*, 025020–025025.
- (37) Guan, Z.; Ni, S. Strain-Controllable High Curie Temperature, Large Valley Polarization, and Magnetic Crystal Anisotropy in a 2D Ferromagnetic Janus VSeTe Monolayer. *ACS Appl. Mater. Interfaces* **2020**, *12*, 53067–53075.
- (38) Guan, Z.; Ni, S. Predicted 2D Ferromagnetic Janus VSeTe Monolayer with High Curie Temperature, Large Valley Polarization and Magnetic Crystal Anisotropy. *Nanoscale* **2020**, *12*, 22735–22742.
- (39) Huang, C.; Feng, J.; Wu, F.; Ahmed, D.; Huang, B.; Xiang, H.; Deng, K.; Kan, E. Toward Intrinsic Room-Temperature Ferromagnetism in Two-Dimensional Semiconductors. *J. Am. Chem. Soc.* **2018**, *140*, 11519–11525.
- (40) Klein, D. R.; et al. Enhancement of Interlayer Exchange in an Ultrathin Two-Dimensional Magnet. *Nat. Phys.* **2019**, *15*, 1255–1260.
- (41) Sivasdas, N.; Okamoto, S.; Xu, X.; Fennie, C. J.; Xiao, D. Stacking-Dependent Magnetism in Bilayer CrI₃. *Nano Lett.* **2018**, *18*, 7658–7664.
- (42) Chen, S.; Huang, C.; Sun, H.; Ding, J.; Jena, P.; Kan, E. Boosting the Curie Temperature of Two-Dimensional Semiconducting CrI₃ Monolayer through Van Der Waals Heterostructures. *J. Phys. Chem. C* **2019**, *123*, 17987–17993.
- (43) Gao, Y.; Wang, J.; Li, Z.; Yang, J.; Xia, M.; Hao, X.; Xu, Y.; Gao, F. On the Ferromagnetism and Band Tailoring of CrI₃ Single Layer. *Phys. Status Solidi RRL* **2019**, *13*, No. 1800410.
- (44) Dolui, K.; Petrović, M. D.; Zollner, K.; Plecháč, P.; Fabian, J.; Nikolić, B. K. Proximity Spin–Orbit Torque on a Two-Dimensional Magnet within Van Der Waals Heterostructure: Current-Driven Antiferromagnet-to-Ferromagnet Reversible Nonequilibrium Phase Transition in Bilayer CrI₃. *Nano Lett.* **2020**, *20*, 2288–2295.
- (45) Hou, Y.; Kim, J.; Wu, R. Magnetizing Topological Surface States of Bi₂Se₃ with a CrI₃ Monolayer. *Sci. Adv.* **2019**, *5*, No. eaaw1874.
- (46) Yang, K.; Hu, W.; Wu, H.; Whangbo, M.-H.; Radaelli, P. G.; Stroppa, A. Magneto-Optical Kerr Switching Properties of (CrI₃)₂ and (CrBr₃/CrI₃) Bilayers. *ACS Appl. Electron. Mater.* **2020**, *2*, 1373–1380.
- (47) Zhang, Z.; Shang, J.; Jiang, C.; Rasmita, A.; Gao, W.; Yu, T. Direct Photoluminescence Probing of Ferromagnetism in Monolayer Two-Dimensional CrBr₃. *Nano Lett.* **2019**, *19*, 3138–3142.
- (48) Bykovetz, N.; Hoser, A.; Lin, C. L. Critical Region Phase Transitions in the Quasi-2D Magnet CrCl₃. *AIP Advances* **2019**, *9*, No. 035029.
- (49) Webster, L.; Yan, J.-A. Strain-Tunable Magnetic Anisotropy in Monolayer CrCl₃, CrBr₃, and CrI₃. *Phys. Rev. B* **2018**, *98*, DOI: 10.1103/PhysRevB.98.144411.
- (50) Wang, Y.; Lv, J.; Zhu, L.; Ma, Y. Crystal Structure Prediction Via Particle-Swarm Optimization. *Phys. Rev. B* **2010**, *82*, No. 094116.
- (51) Kresse, G.; Furthmüller, J. Efficiency of Ab-Initio Total Energy Calculations for Metals and Semiconductors Using a Plane-Wave Basis Set. *Comput. Mater. Sci.* **1996**, *6*, 15–50.
- (52) Perdew, J. P.; Burke, K.; Ernzerhof, M. Generalized Gradient Approximation Made Simple. *Phys. Rev. Lett.* **1996**, *77*, 3865–3868.
- (53) Heyd, J.; Scuseria, G. E.; Ernzerhof, M. Hybrid Functionals Based on a Screened Coulomb Potential. *J. Chem. Phys.* **2003**, *118*, 8207–8215.
- (54) Heyd, J.; Scuseria, G. E.; Ernzerhof, M. Erratum: “Hybrid Functionals Based on a Screened Coulomb Potential” [*J. Chem. Phys.* **118**, 8207 (2003)]. *J. Chem. Phys.* **2006**, *124*, 219906.
- (55) Liechtenstein, A. I.; Anisimov, V. I.; Zaanen, J. Density-Functional Theory and Strong Interactions: Orbital Ordering in Mott-Hubbard Insulators. *Phys. Rev. B* **1995**, *52*, R5467–R5470.
- (56) Togo, A.; Tanaka, I. First Principles Phonon Calculations in Materials Science. *Scr. Mater.* **2015**, *108*, 1–5.
- (57) Nosé, S. A Unified Formulation of the Constant Temperature Molecular Dynamics Methods. *J. Chem. Phys.* **1984**, *81*, 511–519.
- (58) Kvashnin, Y. O.; Bergman, A.; Liechtenstein, A. I.; Katsnelson, M. I. Relativistic Exchange Interactions in CrX₃ (X = Cl, Br, I) Monolayers. *Phys. Rev. B* **2020**, *102*, 115162–115172.
- (59) Henkelman, G.; Arnaldsson, A.; Jónsson, H. A Fast and Robust Algorithm for Bader Decomposition of Charge Density. *Comput. Mater. Sci.* **2006**, *36*, 354–360.
- (60) Anderson, P. W. Antiferromagnetism. Theory of Superexchange Interaction. *Phys. Ther. Rev.* **1950**, *79*, 350–356.
- (61) Goodenough, J. B. Theory of the Role of Covalence in the Perovskite-Type Manganites [La, M (II)]MnO₃. *Phys. Ther. Rev.* **1955**, *100*, 564–573.
- (62) Kanamori, J. Superexchange Interaction and Symmetry Properties of Electron Orbitals. *J. Phys. Chem. Solid* **1959**, *10*, 87–98.
- (63) Guan, Z.; Luo, N.; Ni, S.; Hu, S. Tunable Electronic and Magnetic Properties of Monolayer and Bilayer Janus Cr₂Cl₃I₃: A First-Principles Study. *Mater. Adv.* **2020**, *1*, 244–253.
- (64) Xiang, H. J.; Wei, S.-H.; Whangbo, M. H. Origin of the Structural and Magnetic Anomalies of the Layered Compound SrFeO₂: A Density Functional Investigation. *Phys. Rev. Lett.* **2008**, *100*, No. 167207.
- (65) Lu, X.; Fei, R.; Yang, L. Curie Temperature of Emerging Two-Dimensional Magnetic Structures. *Phys. Rev. B* **2019**, *100*, No. 205409.
- (66) Bogdanov, A. N.; Dragunov, I. E. Metastable States, Spin–Reorientation Transitions, and Domain Structures in Planar Hexagonal Antiferromagnets. *Low Temp. Phys.* **1998**, *24*, 852–857.
- (67) Zhang, S. Q.; Xu, R. Z.; Duan, W. H.; Zou, X. L. Intrinsic Half-Metallicity in 2D Ternary Chalcogenides with High Critical Temperature and Controllable Magnetization Direction. *Adv. Funct. Mater.* **2019**, *29*, No. 1808380.
- (68) Abramchuk, M.; Jaszewski, S.; Metz, K. R.; Osterhoudt, G. B.; Wang, Y.; Burch, K. S.; Tafti, F. Controlling Magnetic and Optical Properties of the Van Der Waals Crystal CrCl_{3-x}Br_x Via Mixed Halide Chemistry. *Adv. Mater.* **2018**, *30*, No. 1801325.
- (69) Ashton, M.; Gluhovic, D.; Sinnott, S. B.; Guo, J.; Stewart, D. A.; Hennig, R. G. Two-Dimensional Intrinsic Half-Metals with Large Spin Gaps. *Nano Lett.* **2017**, *17*, 5251–5257.
- (70) Zhuang, H. L.; Hennig, R. G. Stability and Magnetism of Strongly Correlated Single-Layer VS₂. *Phys. Rev. B* **2016**, *93*, No. 054429.
- (71) Kim, J.; Kim, K.-W.; Kim, B.; Kang, C.-J.; Shin, D.; Lee, S.-H.; Min, B.-C.; Park, N. Exploitable Magnetic Anisotropy of the Two-Dimensional Magnet CrI₃. *Nano Lett.* **2020**, *20*, 929–935.
- (72) Luo, N.; Si, C.; Duan, W. Structural and Electronic Phase Transitions in Ferromagnetic Monolayer VS₂ Induced by Charge Doping. *Phys. Rev. B* **2017**, *95*, No. 205432.
- (73) Guan, Z.; Ni, S.; Hu, S. First-Principles Study of 3d Transition-Metal-Atom Adsorption onto Graphene Embedded with the Extended Line Defect. *ACS Omega* **2020**, *5*, 5900–5910.
- (74) Guan, Z.; Wang, J.; Huang, J.; Wu, X.; Li, Q.; Yang, J. Metal-Free Magnetism and Half-Metallicity of Carbon Nitride Nanotubes: A First-Principles Study. *J. Phys. Chem. C* **2014**, *118*, 22491–22498.
- (75) Guan, Z.; Ni, S.; Hu, S. Tuning the Electronic and Magnetic Properties of Graphene Flake Embedded in Boron Nitride Nanoribbons with Transverse Electric Fields: First-Principles Calculations. *ACS Omega* **2019**, *4*, 10293–10301.

(76) Ye, J. T.; Inoue, S.; Kobayashi, K.; Kasahara, Y.; Yuan, H. T.; Shimotani, H.; Iwasa, Y. Liquid-Gated Interface Superconductivity on an Atomically Flat Film. *Nat. Mater.* **2010**, *9*, 125–128.